

A comparison of climate change simulations produced by two GFDL coupled climate models

Keith W. Dixon*, Thomas L. Delworth, Thomas R. Knutson,
Michael J. Spelman, Ronald J. Stouffer

NOAA—Geophysical Fluid Dynamics Laboratory, PO Box 308, Princeton University Forrestal Campus, Princeton, NJ 08542, USA

Received 20 July 2001; accepted 6 July 2002

Abstract

The transient responses of two versions of the Geophysical Fluid Dynamics Laboratory (GFDL) coupled climate model to a climate change forcing scenario are examined. The same computer codes were used to construct the atmosphere, ocean, sea ice and land surface components of the two models, and they employ the same types of sub-grid-scale parameterization schemes. The two model versions differ primarily, but not solely, in their spatial resolution. Comparisons are made of results from six coarse-resolution R15 climate change experiments and three medium-resolution R30 experiments in which levels of greenhouse gases (GHGs) and sulfate aerosols are specified to change over time. The two model versions yield similar global mean surface air temperature responses until the second half of the 21st century, after which the R15 model exhibits a somewhat larger response. Polar amplification of the Northern Hemisphere's warming signal is more pronounced in the R15 model, in part due to the R15's cooler control climate, which allows for larger snow and ice albedo positive feedbacks. Both models project a substantial weakening of the North Atlantic overturning circulation and a large reduction in the volume of Arctic sea ice to occur in the 21st century. Relative to their respective control integrations, there is a greater reduction of Arctic sea ice in the R15 experiments than in the R30 simulations as the climate system warms. The globally averaged annual mean precipitation rate is simulated to increase over time, with both model versions projecting an increase of about 8% to occur by the decade of the 2080s. While the global mean precipitation response is quite similar in the two models, regional differences exist, with the R30 model displaying larger increases in equatorial regions.

© 2003 Elsevier Science B.V. All rights reserved.

Keywords: global change; global circulation models; global warming; precipitation; thermohaline circulation; sea ice

1. Introduction

Results of climate change simulations performed using computer models of the global climate system developed at NOAA's Geophysical Fluid Dynamics

Laboratory (GFDL) have appeared in each of the first three scientific assessment reports of the Intergovernmental Panel on Climate Change (IPCC, 1990, 1996, 2001). These numerical models consist of an atmospheric general circulation model (GCM) coupled to an ocean GCM. Relatively simple models of sea ice and land surface hydrology are also incorporated into the climate models. Two different spatial resolutions have been employed in these GFDL studies, and multiple

* Corresponding author.

E-mail address: kd@gfdl.noaa.gov (K.W. Dixon).

versions of global coupled climate models have been constructed using each of the two sets of resolution characteristics.

Analyses of two of GFDL's coarser resolution "R15" coupled models are included in the most recent IPCC report, as are results from three "R30" models having somewhat higher spatial resolution. None of the models are exactly alike, and therefore, their responses to prescribed climate change forcing scenarios should not be expected to be identical. Each model has its own control simulation, from which climate change experiments have been initialized.

Here, the term "model" refers to a specific configuration of computer code that has produced a multi-century or longer control simulation of the Earth's climate in which external forcings (such as specified atmospheric CO₂ levels, solar irradiance and orbital parameters) are held constant in time. Thus, changes in the computer code, sub-grid-scale parameterization schemes, boundary conditions, etc., can lead to different models that share the same spatial resolution.

In this study, we focus on climate change projections produced by GFDL's most recent R15 and R30 coupled climate models. These two models are identified as GFDL_R15_b and GFDL_R30_c in the IPCC's Third Assessment Report. See Chapter 9, Table 9.1 of the Intergovernmental Panel on Climate Change (IPCC, 2001) report. Some results from the R15 model are presented in Dixon and Lanzante (1999) and the R30 model is described in detail in Delworth et al. (2002). Here, aspects of the two models' global and regional responses to a specific climate forcing scenario are presented and compared. Analyses of changes in annual mean surface air temperatures, Arctic sea ice amounts, precipitation rates and the strength of the North Atlantic meridional overturning circulation are presented.

The GFDL_R15_b and GFDL_R30_c models were constructed from the same computer code, and both use the same physical parameterization schemes. The two models can be thought of as differing mainly in spatial resolution. Other configuration differences between the two include the choice of time steps and sub-grid-scale diffusion and viscosity coefficients (associated with the resolution difference). The specification of some cloud albedo properties differ, as they were fine-tuned in each atmospheric model before being coupled to achieve a global mean radi-

ation balance at the top of the atmosphere. In addition, a gravity-wave drag parameterization, generally considered important to prevent higher resolution atmospheric models from developing circulations that are too zonal (e.g., Boer and Lazare, 1988), is included in the R30 version of the atmospheric model, but not the R15. The details of the initialization techniques employed when combining the individual model components into a working coupled model were similar, but not identical.

While the kinds of model configuration differences noted above are relatively minor compared to the large number of common features shared by the two models, we are aware that seemingly subtle model configuration changes can result in notable changes in the simulated climate. Therefore, we will not automatically assume that differences between the GFDL_R15_b and GFDL_R30_c models' climate change responses arise solely due to differences in spatial resolution. The results presented here document the differences and similarities in climate change responses produced by a pair of coupled climate models that use very similar physical parameterizations, but differ in spatial resolution. They are examples of the kinds of changes that one can see when increases in available computer resources lead to higher resolution coupled climate models, but are not meant to be considered representative or typical of results produced by other coupled climate models that use different dynamical cores, physical parameterizations, numerical schemes, etc.

2. Model overview

2.1. Model configurations and experimental design

A set of six R15 and a set of three R30 climate change experiments are examined here. The designation R15 or R30 derives from the spatial resolution of the atmospheric spectral model component of the global coupled model. The higher resolution R30 (rhomboidal truncation at wave number 30) model has a transform grid spacing of 3.75° longitude by ~ 2.25° latitude (a 96 × 80 global grid). The R15 model's transform grid has 7.5° longitude by ~ 4.5° latitude spacing (a 48 × 40 grid). The R30 atmospheric model has 14 sigma levels spaced unevenly in

the vertical and the R15 model has 9. Topography is determined by projecting observed surface elevations onto spherical harmonics. The R30 model uses the method of Lindberg and Broccoli (1996) to improve the representation of the surface elevation, and thus minimize spurious small-scale precipitation extrema that are more pronounced in models having higher horizontal resolution.

A relative humidity-based cloud prediction scheme and moist convective adjustment (Manabe et al., 1965) are used in the atmospheric model components. Where predicted, clouds are assumed to fill the grid box. Precipitation occurs when water vapor supersaturation is simulated, falling as snow when the temperature of the lower atmosphere is below freezing. Solar irradiance does not vary inter-annually during the model integrations.

For each model resolution, the land model component's horizontal grid matches the atmospheric model's transform grid. At the atmosphere–land surface interface, the sum of the short-wave, long-wave, latent and land–air sensible heat fluxes is assumed zero (i.e., the soil has no heat storage capability, and the land surface temperature is determined diagnostically). A simple bucket hydrology scheme is used for soil moisture calculations, with a uniform field capacity of 0.15 m of liquid water assumed (Manabe, 1969). Evaporation is calculated as the product of the potential evaporation from a surface saturated at the local surface temperature and pressure and an evapotranspiration efficiency factor. Over land, the evaporation efficiency is given by the ratio of local soil moisture to a critical value that is 75% of field capacity, and is set to unity if soil moisture exceeds this critical value. When the soil moisture is at field capacity, excess water added via precipitation or snowmelt is converted to runoff. Runoff from land points is instantaneously routed to the ocean following observed river drainage basins. Similarly, when the model-predicted snow depth exceeds a specified value at a grid point (0.2 m liquid water equivalent), the excess snow is routed to the ocean as runoff.

Each coupled model's ocean model component has the same number of latitude rows as the atmospheric model to which it is coupled and twice as many grid points in the zonal direction (i.e., a 192×80 grid for the R30 ocean and a 96×40 grid for the R15 ocean). There are 18 and 12 unevenly spaced vertical levels in

the R30 and R15 ocean model components, respectively. These *z*-coordinate rigid-lid ocean models are based upon the GFDL Modular Ocean Model version 1 code (Pacanowski et al., 1991) and employ the Cox (1987) implementation of sub-grid-scale isopycnal tracer diffusion.

The horizontal grid spacing of each coupled model's sea ice component matches that of its underlying ocean model. These coupled model experiments use a relatively unsophisticated sea ice model that neglects the internal pressure of the sea ice. Its lineage can be traced back to the model developed by Bryan (1969), although modifications have been made over time, several of which are noted in Manabe et al. (1990). At each grid point, average sea ice thickness is predicted, but not fractional coverage (i.e., the grid cell is either considered completely ice free or entirely covered by ice of some model-predicted thickness). Fluxes involving the latent heat of fusion are conserved within the coupled model system during freezing and melting. In addition, surface water freshening and brine rejection occur in a conservative manner as sea ice melts or forms. Sea ice surface albedos are dependent on the prognostic ice thickness and surface air temperature (Manabe et al., 1991). Snow that falls upon preexisting sea ice is instantly converted into sea ice. The sea ice moves freely with the surface ocean currents, provided the ice thickness is less than 4 m. Additional convergence of sea ice is not permitted at grid points where the thickness exceeds 4 m. Wind stresses computed by the coupled model's atmospheric component are passed to the liquid ocean GCM, without directly interacting with the sea ice.

The coupled models are forced by seasonally varying insolation (no diurnal or inter-annual insolation variations are included). Fluxes of momentum, heat and freshwater between the model's atmosphere–land component and the ocean–sea ice component are computed and exchanged once per day. In an attempt to minimize climate drift, seasonally and spatially varying heat and freshwater fluxes are added to the ocean surface. As described in Manabe et al. (1991), these flux adjustments are determined before the coupled model is initialized, and they do not vary inter-annually.

Coupled model initial conditions for the climate change scenario experiments examined here are drawn from widely spaced points in time in their

respective long-running control integrations. Accordingly, the control integrations are taken to represent preindustrial conditions when compared to the climate change scenario results. A reconstruction of atmospheric greenhouse gas (GHG) levels for the period 1765–1990 is used to force the climate change experiments. The combined effects of well-mixed atmospheric GHGs are modeled as time-varying effective CO₂ amounts. After scenario year 1990, effective CO₂ levels are specified to grow at a 1% per year compounded rate. The direct effect of tropospheric sulfate aerosols is included in the model as spatially and temporally varying changes in surface albedos, following the method used by Haywood et al. (1997). The radiative forcing scenario applied to the models is quite similar to the IS92a scenario (Leggett et al., 1992), often referred to as a business-as-usual scenario. It should be noted that in recent years, actual levels of the well-mixed greenhouse gases have increased at a rate less than the IS92a scenario (Hansen et al., 2000). In the simulations presented here, effective CO₂ concentrations reach levels that are double that of the control in the early 2020s and are four times the control in the early 2090s.

The six R15 climate change experiments examined here were first presented by Dixon and Lanzante (1999) (hereafter DL99). Using the DL99 nomenclature, experiments A1766, B1766, C1766, A1866, B1866 and C1866 are used in the present study. Three of the R15 simulations (the DL99 x1766 experiments) are initialized with radiative forcings representing scenario year 1766 and are integrated for more than three centuries to the 2090s. Assuming the end of year 1765 to be representative of preindustrial conditions, these three experiments experience a smooth transition in radiative forcings when initialized from the control model experiment. All the R30 experiments and three of the R15 runs (the x1866 experiments) are initialized with radiative forcings representing scenario year 1865 or 1866, and thus require 100 fewer years of integration to reach the 2090s than do the x1766 experiments. Upon initialization from their respective control runs, effective CO₂ levels in the six experiments that start in the mid-1860s undergo an instantaneous 6% increase. The magnitude of this instantaneous increase is the difference between the effective CO₂ time series values for 1765 and 1865. Delworth et al. (2002) provide addi-

tional documentation regarding the configuration and climate simulations produced by the R30 model studied here.

DL99 showed that projections of 21st century surface air temperatures and the strength of the North Atlantic overturning were insensitive to whether the scenario experiments were initialized with 1765 or 1865 conditions, providing some justification for the substantial savings of computer time realized by conducting the shorter experiments. Analyses presented here will focus on the period extending from the mid-20th century to the late 21st century, thereby reducing the probability that they could be substantially influenced by effects similar to the cold start problem described by Hasselmann et al. (1993).

2.2. Previous model studies

Since this study focuses upon comparing the responses of the GFDL_R15_b and GFDL_R30_c climate models to increasing levels of atmospheric GHGs and tropospheric aerosols, a partial listing of publications that document aspects of one or both of the models is presented below.

Characteristics of the GFDL_R15_b model's global mean surface air temperature (SAT) and North Atlantic thermohaline circulation (THC) responses to climate change forcings were first described by DL99. Dixon et al. (1999) found that GHG-induced changes in surface freshwater fluxes are the predominant reason that the R15 model's THC weakens in global warming experiments, with surface heat flux changes being of secondary importance and wind stress changes having negligible impact. Analyses of the R15 model's Arctic oscillation and related surface fluxes have revealed that GHG-induced THC weakening could be delayed by several decades in response to a sustained upward trend in the Arctic/North Atlantic oscillation during winter, such as has been observed from the 1960s to the 1990s (Delworth and Dixon, 2000).

Anthropogenically induced sea level change projections diagnosed from both the GFDL_R15_b and GFDL_R30_c experiments are presented in Gregory et al. (2001). The two models produce very similar projections for global mean sea level changes arising from the thermal expansion of seawater. Comparison of the geographic patterns of 21st century sea level

change simulated in the two models yields a 0.63 correlation coefficient.

Analyses of late 20th century ocean heat content changes simulated in some GFDL_R30_c experiments are included in Levitus et al. (2001). Model runs with transient climate change forcings were found to be generally consistent with observed global ocean heat content changes for the period from the 1950s to the 1990s. The amount of unforced global ocean heat content variability produced in the control model suggests that random fluctuations of the climate system are unlikely to produce an increase as large as that observed. In addition, in an investigation of positive trends in the probability of great floods associated with anthropogenic climate change, Milly et al. (2002) report that observations are consistent with the results of a set of R30 experiments.

The nature of the internally generated model variability displayed in an ensemble of GFDL_R30_b simulations described in Knutson et al. (1999) and Delworth and Knutson (2000) is broadly similar to that exhibited in the set of GFDL_R30_c experiments studied here. The Delworth and Knutson (2000) results suggest that internally generated multi-decadal variability of the coupled ocean–atmosphere system, along with changing radiative forcing, could have played a major role in producing the magnitude and pattern of warming observed in the early 20th century. Such findings demonstrate the value of performing multiple climate change experiments with a single model—a conclusion also borne out in DL99.

We note that the surface air temperatures of the initial conditions used for these R15 experiments exhibit a cold bias, especially in these high latitudes of the Southern Hemisphere. The cold bias developed as the modeled climate drifted during the first several hundred years following the initialization of the GFDL_R15_b control model. In their review of coupled model initialization techniques, Stouffer and Dixon (1998) defined climate drift as an unforced trend away from some initial state, with the trend not being part of normally occurring variability about a constant mean state. While reducing the amount of drift that might otherwise take place, flux adjustments do not guarantee that no drift will occur. Drift such as that seen in the GFDL_R15_b control model can occur because the fully coupled model includes feedbacks and time scales of variability that are not

present in the stand-alone atmosphere and ocean model integrations used to initialize the coupled model and determine the flux adjustments.

The R15 climate change experiments examined here start from points more than 1000 years after the control model was initialized. By this time, the rate of climate drift is quite small, but the accumulated drift over many centuries has produced a noticeably cooler climate. Neither the older GFDL_R15_a control model (Manabe et al., 1991) nor the R30 control models exhibit drifts of the magnitude and kind seen in the first several hundred years of the GFDL_R15_b case. Little climate drift occurs during the later segments of the GFDL_R15_b control run examined here, with the trend in global mean surface air temperatures varying between -0.06 and $+0.05$ K century⁻¹. Likewise, the portion of the GFDL_R30_c control run studied here exhibits a slight drift of -0.04 K century⁻¹.

3. Responses to climate change forcings

3.1. Surface air temperature (SAT)

3.1.1. Global mean SAT response

The ensemble averaged global mean SAT responses for the R15 and R30 experiments are similar, especially during the 20th and early 21st centuries (Fig. 1, solid lines). Compared to their respective control experiments, the climate change scenario experiments warm ~ 0.5 K by the decade of the 1950s and ~ 1.3 K by the decade 2000–2009. More specifically, the 1950s ensemble mean global SAT warming response for the six R15 experiments is 0.45 K, with the six ensemble members ranging between 0.40 and 0.56 K. For the same period, the mean warming for the three R30 simulations is 0.48 K, with the responses of the three members ranging from 0.41 to 0.56 K. Five decades later, the R15 ensemble mean global warming is 1.30 K, with individual ensemble members ranging from 1.26 to 1.35 K, and the R30 ensemble mean response is 1.34 K, with an intra-ensemble range of 1.28–1.44 K. For comparison, the standard deviation of the time series of global annual mean SATs is 0.10 K for the R15 control model and 0.14 K for the R30 control model.

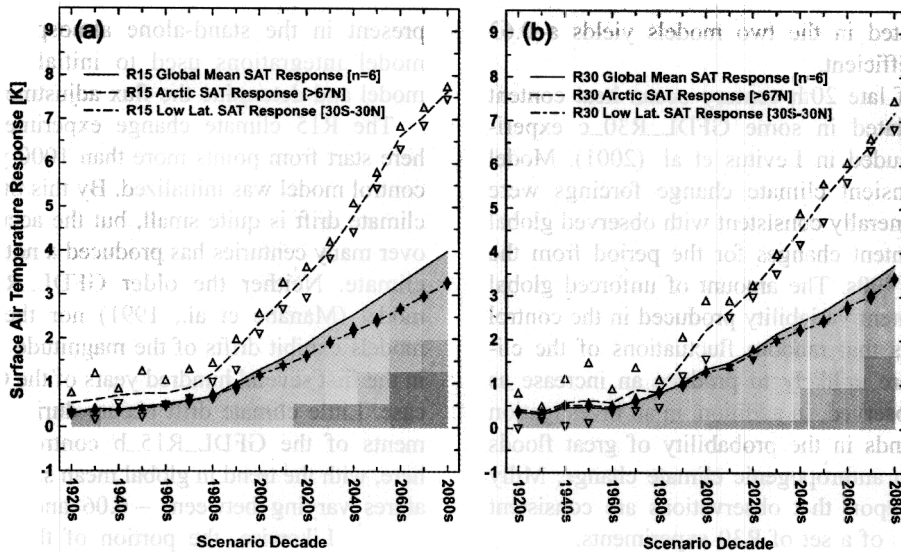


Fig. 1. Time varying decadal mean surface air temperature responses simulated by (a) the R15 set of six climate change experiments and (b) the R30 set of three climate change experiments. Ensemble mean globally averaged SAT responses are indicated by solid lines and shaded areas. Ensemble mean SAT responses averaged over the region poleward of 67°N are shown as dashed lines. Ensemble mean low latitude (30°S–30°N) SAT responses are indicated by dash-dot lines. Upward and downward pointing triangles indicate the maximum and minimum SAT responses of the individual ensemble members (open triangles for Arctic, solid for low latitudes). SAT responses for each experiment are computed by subtracting a measure of its respective control model's SAT (least-squares regression lines fitted through the control model's annual mean time series) from the climate change experiment's annual mean SAT time series.

The R15 model's global mean SAT response is somewhat greater than that of the R30 model integrations during the latter portion of the 21st century. For the four decades beginning with the 2050s, the decadal averages of all six of the R15 ensemble members exhibit a larger warming response than each of the three R30 simulations. Averaged over the 40-year period extending from scenario years 2050–2089, the ensemble mean global SAT response of the R15 runs is 0.26 K greater than the R30 ensemble mean.

Why the R15 experiments warm somewhat more rapidly during the latter portion of the 21st century is not known with certainty. We can state that the bulk of the differences between the 21st century SAT responses of the R15 and R30 models are not due to any residual cold start bias that might be associated with three of the R15 experiments having had their transient forcing begin with 1766 conditions rather than 1866. During the 21st century, the difference between the R15 and R30 models' global mean SAT responses is approximately three times greater than the difference between the R15 x1766 experiments ensemble mean and that of the trio of R15 x1866 experiments.

Note that in this paper, figures showing time series of decadal means purposely begin with the 1920s rather than 1870s. This reflects the judgment that adjustments within the modeled climate system during the half century leading up to 1920 are sufficient such that any potential cold start biases are no longer readily obvious.

That the R15 and R30 models' control climates differ may be a factor responsible for many of the differences in the two models' SAT responses. It has been demonstrated that a numerical model's climate sensitivity (typically defined as the amount of global mean SAT warming realized when a model equilibrates to a doubling of atmospheric CO₂) can be related to the mean state of a model's unperturbed or control climate (Spelman and Manabe, 1984). All else being equal, the cooler the control climate, the larger the expected warming response to increasing levels of GHGs, since more opportunities for positive feedbacks exist when more extensive snow and ice are present. As is discussed in more detail in the following sections, the R15 model's control surface climate is cooler than the R30 model's, with the R15 model

simulating markedly more Southern Hemisphere sea ice. Examining an atmospheric GCM coupled to a mixed layer ocean with thermodynamic sea ice, Rind et al. (1997) found that increased control-run sea ice coverage in the Southern Hemisphere enhanced the temperature sensitivity to a doubling of atmospheric CO₂. The larger warming response seen in the R15 climate change experiments is qualitatively consistent with the difference in the two models' control climates, but the magnitude of this effect has not been determined quantitatively.

The individual ensemble members' global mean SAT responses do not become more tightly clustered as the simulated climate changes, nor do they diverge. For the six R15 ensemble members, differences between the largest and smallest decadal mean responses vary from 0.08 to 0.32 K for the period shown in Fig. 1. In part because of its smaller ensemble size, the range of the R30 decadal mean SAT responses is less than that of the R15, never exceeding 0.21 K.

3.1.2. Polar amplification of the SAT response

Arctic surface air temperatures warm relatively rapidly in both the R15 and R30 climate change experiments, reducing the equator to pole temperature gradient. Fig. 2 depicts temporal variations of a measure of the extent of the Northern Hemisphere polar amplification signal, namely, the ratio of the SAT response poleward of 67°N divided by the SAT response of the latitude band from 30°S to 30°N. This measure of the polar amplification signal grows over time for the R15 and R30 climate change experiments. Compared to their respective control integrations, the annual mean SAT difference between these two latitude bands is reduced by ~4.4 K (R15 ensemble mean) and ~3.8 K (R30 ensemble mean) by the decade of the 2080s.

The R15 model exhibits a somewhat greater Northern Hemisphere polar amplification signal than does the R30 model. Compared to the R30 experiments, the R15 runs tend to exhibit more SAT warming in the Arctic and slightly less warming in low latitudes; both factors contributing towards the R15 polar amplification ratios being larger than the R30s, as seen in Fig. 2. For the decade 2000–2009 and all subsequent decades, the ensemble mean warming of the R15 model's Arctic SATs is more than twice as great as that simulated for the half of the Earth's surface that

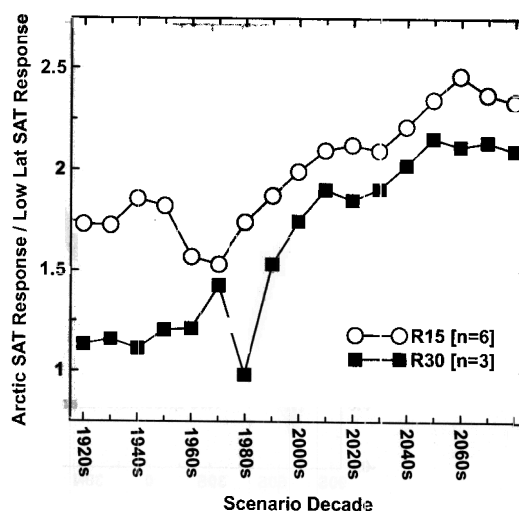


Fig. 2. Time variations in the strength of the Northern Hemisphere polar amplification signal as measured by the ratio of the SAT response of the region 67°N–90°N to the SAT response of the region 30°S–30°N. Values for the R15 (open circles) and R30 (solid squares) climate change experiments are calculated from ensemble mean decadal averages shown in Fig. 1.

lies between 30°S and 30°N. Decadal mean polar amplification ratios for the R30 ensemble exceed 2.0 from the 2040s onward.

The polar amplification seen in the Northern Hemisphere of these GFDL models is not unlike that seen in several other model simulations conducted at other research centers, as evident in Fig. 3 of Räisänen (2001). The ice/snow albedo positive feedback mechanism contributes to this phenomenon in the GFDL model simulations. An initial warming can cause melting, thereby reducing the total surface area covered by snow and ice. As surfaces take on the lower albedo of the underlying land (or water) surface, more incoming solar radiation is absorbed at the surface. Some of this additional energy is transferred to sensible heating of the lower atmosphere (or surface waters), which in turn can induce additional melting of snow and ice.

When sufficient insolation is present, the mechanism described above is more efficient over land than over the ocean because one can expect a larger fraction of the absorbed insolation to be converted to atmospheric sensible heat over a land surface. However, if an initial warming causes a reduction in polar sea ice coverage, then additional warming of the surface air

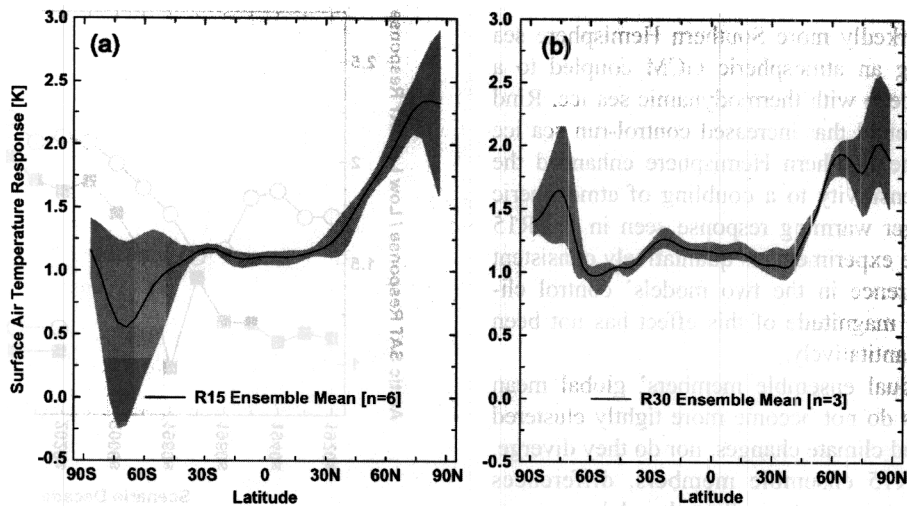


Fig. 3. Zonal mean SAT responses for the (a) R15 and (b) R30 climate change experiments averaged over the scenario time period 1990–2014. Ensemble mean values are shown by the solid black line. Gray areas encompass the range of SAT responses produced by the ensemble members. For each climate change experiment, SAT responses were calculated by averaging zonal mean SATs over the period of interest, and then subtracting the zonal mean SATs averaged over the corresponding 25-year period of the control model. Ensemble means were calculated by averaging the SAT responses of the six R15 and three R30 experiments.

can be expected via a different mechanism. Since the removal of the insulating sea ice permits much more heat to pass from the ocean to the atmosphere, especially during winter, SATs warm relative to what would otherwise be the case. However, sea ice dynamics and the effect of meltwater on ocean circulation may diminish the feedback. Model studies have shown that the magnitude of the sea ice feedback is dependent upon the details of the sea ice model formulation and the control model's sea ice distribution (e.g., Ingram et al., 1989; Rind et al., 1995, 1997).

The finding that the global mean, annual mean SAT responses of the two GFDL models are similar, but some differences exist in the extent of the polar amplification of the surface warming, is broadly consistent with analyses of the response of a pair of Hadley Centre models of different resolution to increased levels of atmospheric carbon dioxide (Senior, 1995) and the response of the ECHAM4 model at different resolutions (May and Roeckner, 2001). As is the case in this study of the GFDL models, the lower resolution Hadley Centre and ECHAM4 models exhibit larger wintertime polar amplification signals than their higher resolution companions. Senior also attributed the different equilibrium responses of the two Hadley Centre models to

differences in the control models' sea ice simulations and the related influences on the sea ice albedo feedback effect. May and Roeckner speculated that the warmer present-day climate simulated in their high-resolution atmospheric model led to less snow cover and thus a less effective albedo feedback than in their lower resolution coupled model. That the lower resolution GFDL, Hadley Centre and ECHAM4 control models all produce climates that are predisposed to yield stronger albedo feedbacks than their respective higher resolution companion models may be fortuitous and not directly related to resolution differences. Additional experiments are under consideration to better quantify the role of albedo feedback mechanisms on the GFDL models' climate sensitivity.

3.1.3. Spatial variations in SAT responses

Figs. 3 and 4 depict how the R15 and R30 zonal mean SAT responses vary with latitude for two 25-year periods (1990–2014 and 2065–2089). The response is defined as the change relative to the respective control model integration. The earlier time period (Fig. 3) was selected because it contains the present, and the later period (Fig. 4) was chosen because it includes the end of the model integrations when the climate response is greatest. Maps of the

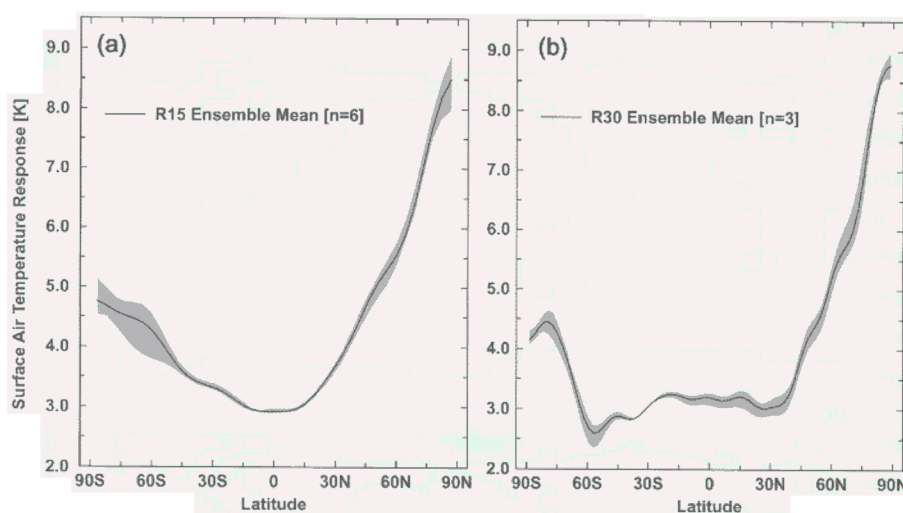


Fig. 4. Same as Fig. 3, but averaged for the time period 2065–2089. Note that y-axis scale differs from that used in Fig. 3.

geographical variations in modeled SAT responses for the 25-year period 2065–2089 appear in Fig. 5.

The results of the R15 and R30 models are broadly similar over latitudes ranging from $\sim 30^{\circ}\text{S}$ to the North Pole. Strong warming over the Arctic and the northernmost continental regions is a feature common to both models, as is a relative minimum located in the North Atlantic between 50°N and 60°N . South of $\sim 40^{\circ}\text{S}$, the two models respond somewhat differently to the transient radiative forcing scenario. Some differences also exist in the tropical Pacific, where the pattern of enhanced warming of sea surface temperatures (SSTs) and SATs resembles the R30 model's El Niño state, as was discussed by Knutson and Manabe (1998) for the earlier GFDL_R30a model version. In addition, in the R30 scenarios, a larger difference exists between the SAT responses over the North Atlantic and North Pacific than in the R15 ensemble.

Interpolating the R30 ensemble mean SAT response results to the R15 grid and then computing the pattern correlation with the R15 model yields an overall global spatial correlation of 0.77 for the 2065–2089 time period. The correlation of the R15 and R30 SAT responses over the domain extending from 40°S to 90°N is 0.86 for this period.

The general pattern of the R30 experiments' zonally averaged SAT responses is similar during both of the 25-year periods shown (Figs. 3b and 4b). The smallest zonally averaged warming responses are

found at $\sim 57^{\circ}\text{S}$. Zonal mean SATs in the latitude range of $\sim 20^{\circ}\text{N}$ – 37°N warm more slowly than elsewhere in the Northern Hemisphere. The largest zonal mean warming responses are found in the high latitudes of both hemispheres, with the Arctic warming being the greatest, especially during the 2065–2089 period. A large increase in warming poleward of $\sim 60^{\circ}\text{N}$ emerges during the late 21st century. Although more experiment-to-experiment variations are seen in the high latitudes during the earlier of the two 25-year periods, there is no significant change in inter-experiment variability.

An especially large amount of inter-experiment variability is seen in the R15 model's SATs in the higher latitudes of the Southern Hemisphere. This is associated with a low-frequency oscillation that occurs in the R15 model's Pacific sector of the Southern Ocean and the Ross Sea. This feature, which has a characteristic time scale of more than a century, is not believed to have a real-world counterpart, and has not been as prevalent a feature in GFDL's other R15 and R30 coupled climate models. The presence of this feature in the R15 control run is believed to be linked to ocean simulation deficiencies. In particular, the R15 control integration develops more extensive Southern Hemisphere sea ice coverage than is observed (and more than in the R30 model). Additionally, this region of R15 model's ocean is less stratified than observed. The low-frequency SAT variability associated with this model

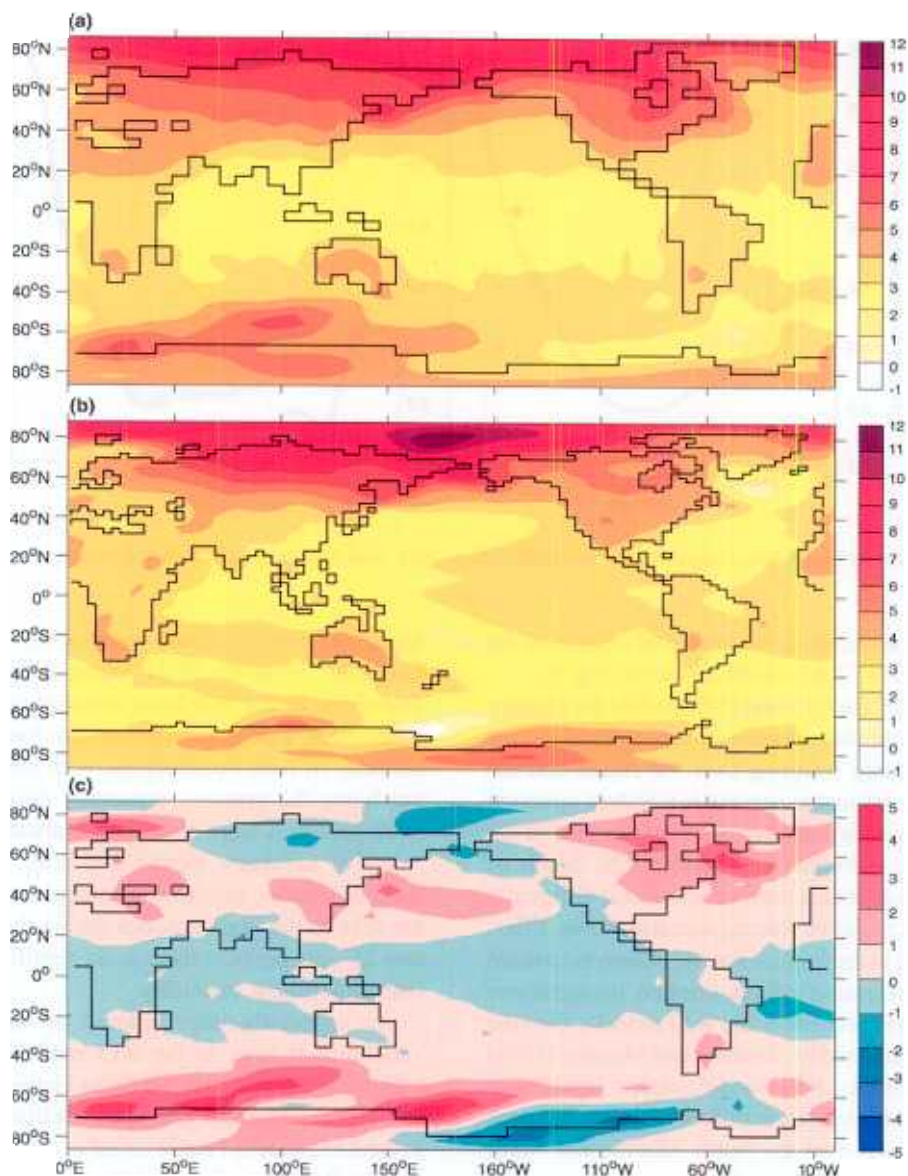


Fig. 5. Annual mean surface air temperature responses for the period 2065–2089, averaged over (a) the six R15 climate change experiments and (b) the three R30 climate change experiments. The difference (R15 – R30) is shown in (c). The R30 results were interpolated to the R15 grid before differencing. The contour interval is 1.0 K.

phenomenon also contributes to the experiment-to-experiment range of responses referred to in Section 3.1.1.

For the period 1990–2014, much less of a warming response is seen in the southern high latitudes of the R15 experiments than in the R30 runs. However, during the 2065–2089 period, the R15's southern

high-latitude warming is greater than the R30's. Having started with more southern sea ice, the R15 simulations have more opportunity for positive ice feedbacks as the transient radiative forcing grows in the 21st century. In addition, the freshening of surface waters associated with the melting of more southern sea ice in the R15's experiments contributes toward

Table 1

Standard deviations of the annual mean surface air temperature time series for the R15 and R30 control models

	R15 (in K)	R30 (in K)
Global		0.14
Northern Hemisphere		0.17
Southern Hemisphere		0.14
Low latitudes (30°S–30°N)		0.19
Arctic (>67°N)		0.54

increasing the ocean stratification, which reduces the Southern Ocean ventilation processes that take up and sequester excess (GHG-related) atmospheric heat.

In the R15 and R30 model experiments, the warming response in the Southern Hemisphere's high-latitudes lags that projected to occur in the northern polar region. This interhemispheric asymmetry has been noted previously in transient climate change studies at GFDL (Bryan et al., 1988; Stouffer et al., 1989) and elsewhere. The interhemispheric asymmetry has been linked to air–sea heat exchange in the Southern Ocean. The thermal inertia is in part related to greater ocean surface area existing in the Southern Hemisphere than in the Northern Hemisphere. Additionally, areas of very deep and rapid vertical mixing are simulated in the models' Southern Ocean (perhaps more so than actually occurs). This extensive amount

of ocean ventilation provides the atmosphere with a large reservoir of water with which to equilibrate. Deep ocean mixing processes in both hemispheres introduce multi-century or longer equilibration time scales to the global climate system. As an illustration of the lag introduced by deep ocean mixing, experiments conducted at R15 resolution suggest that global mean SATs would ultimately equilibrate at a level ~ 1.0 K warmer than present if GHG and tropospheric sulfate aerosol levels were to remain fixed in time at current levels (Wetherald et al., 2001).

As shown in Table 1, somewhat more year-to-year variability is present in the R30 control model's time series of annual mean, global mean SATs, than is the case for the R15 control model segments studied here ($\sigma = 0.10$ K for the R15 and $\sigma = 0.14$ K for the R30). That the R30's tropical SAT variability exceeds the R15's largely stems from the R30 model producing an ENSO-like phenomenon of similar magnitude as that which is observed. However, deficiencies exist in the spatial pattern of the R30 model's ENSO and in the unrealistically long (~ 8 – 9 -year) time scale of the modeled oscillation (Delworth et al., 2002). The amplitude of the ENSO-like feature in the GFDL_R15_b model studied here is much less than observed, as was the case for the earlier GFDL_R15_a control model (Knutson et al., 1997). The standard deviation of the

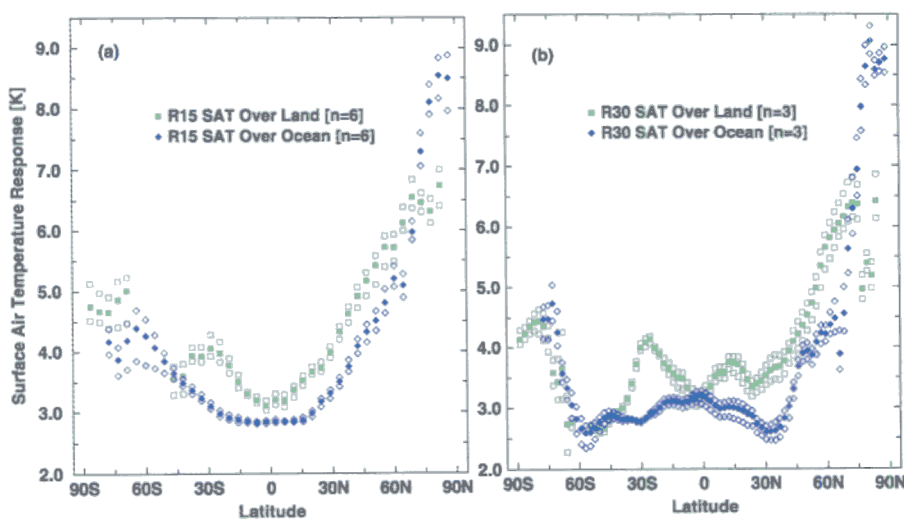


Fig. 6. Zonal mean SAT responses computed over land (green squares) and sea (blue diamonds) for the (a) R15 and (b) R30 climate change experiments averaged over years 2065–2089. Solid squares and diamonds represent the ensemble mean value. Open squares and diamonds show the range of SAT responses produced by the ensemble members.

R30's Arctic SAT time series is somewhat larger than that of the R15 control run. In the R30 model, the Northern Hemisphere SAT variability is greater than that of the Southern Hemisphere, while the reverse is true for the R15 model, due to the previously mentioned spurious low-frequency variability present in the R15 model's Southern Ocean region.

As apparent in Fig. 5, for a given latitude, modeled temperature increases tend to be more pronounced over land than over the ocean. However, this relationship does not hold everywhere. Fig. 6 shows the two models' zonally averaged SAT responses over land and sea for the period 2065–2089 (same time period as Figs. 4 and 5). Note that in both models, the zonal mean SAT responses are most similar over land and ocean near the equator. In addition, as Arctic sea ice melts in the climate change scenario, surface air temperatures over the high northern oceans exhibit a larger warming response than that seen over the northernmost land areas. Strong warming over the high-latitude oceans can be attributed in part to the large fluxes of heat from the ocean to the atmosphere that emerge when insulating sea ice melts away.

The R15 model's zonal mean temperature responses yield smoother curves (Fig. 6) than do those produced in the R30 climate change simulations. Relative minima in ocean surface warming that appear at $\sim 57^\circ\text{S}$ and 30°N in the R30 are not evident in the R15 results. The smoother R15 results are in part related to higher amounts of sub-grid-scale diffusion in the lower resolution ocean model. That the R30 model exhibits an El Niño-like pattern in the SST response to the climate change forcing contributes to low-latitude variations.

4. Arctic sea ice volume

Sea ice thickness, but not fractional coverage, is predicted by the model's sea ice code, which includes simple ice thermodynamics and advection by surface ocean currents. Northern Hemisphere sea ice extent as simulated in a climate change experiment conducted using the earlier GFDL_R15_a model was reported by Vinnikov et al. (1999). In that study, good agreement with observations was found for both the model's mean sea ice extent and the decrease in coverage seen during the second half of the 20th century.

For the relatively simple sea ice model employed in the GFDL coupled model calculations, the interplay between high-latitude spatial filtering and the criterion selected for the binary determination of whether a grid cell is covered by sea ice or not can complicate the definition of sea ice extent and its variability (Moritz and Bitz, 2000). Here, these potential complicating factors are largely avoided by examining annual mean sea ice volume, as opposed to the areal extent of sea ice coverage. In addition, spatial filtering is limited to latitude rows poleward of $\sim 68^\circ$ in the two models studied here, while the filtering extended to $\sim 51^\circ$ latitude in the Vinnikov et al. experiment.

Using data collected from submarines, Rothrock et al. (1999) estimated that the volume of Arctic sea ice in the 1990s was only $\sim 60\%$ of that which existed two to four decades earlier. However, numerical ice–ocean modeling studies by Holloway and Sou (2001) suggest that the magnitude of the decrease seen by Rothrock et al. may have been biased by the sampling (location and time) associated with the submarine cruise tracks, as a redistribution of sea ice within the Arctic may have occurred during the period examined. The Holloway and Sou modeling studies yield a more modest 12% reduction of sea ice over the entire Arctic compared to a 45% loss of sea ice when the model was sampled at only the submarine locations. This compares quite favorably with the 48% reduction observed at these same submarine stations. Winsor (2001) reported that the Arctic ice did not continue to thin during the 1990s, contrary to some preliminary evidence offered by Rothrock et al. Because the observational record of Arctic sea ice thickness is quite limited in both spatial and temporal sampling, uncertainties remain regarding the characteristics of its multi-decadal natural variability and to what extent the recent observed trends may be attributed to anthropogenic forcing or natural variability.

In the R30 control simulation, annual mean values of sea ice volume poleward of 67°N do not deviate by more than 20% from the long-term mean, and decadal averages all lie within 16% of the mean. The R15 control model's Arctic sea ice is somewhat less variable than the R30's. The standard deviation of the annual mean sea ice volume poleward of 67°N is 25% greater in the R30 control model than in the R15 control model. Note that as a result of the climate drift that took place during the first thousand years after

coupling, the annual mean volume of Arctic sea ice in the R15 control model studied is ~ 25 – 30% greater than that simulated in the R30 control run.

Fig. 7 depicts the decadal variations of the annual mean volume of Arctic sea ice simulated in the R15 and R30 climate change experiments. When compared to their respective control integrations, more Arctic sea ice is lost in the R15 climate change experiments than in the R30 model simulations. This is true whether the change is expressed as a percentage of the control run (as in Fig. 7) or in absolute terms. From the decade of the 2020s onward, each of the six R15 climate change experiments has lost a larger percentage of its Arctic sea ice volume than have any of the three R30 runs. Although the R15 experiments' initial Arctic sea ice volume average is greater than the R30s', the more rapid loss of ice that occurs in the R15 model results in less Arctic sea ice remaining in the R15 experiments by the end of the climate change simulations. From the 2040s onward, the ensemble mean absolute volume of Arctic sea ice simulated to exist in the R30 climate change experiments is greater than that simulated in the R15 runs.

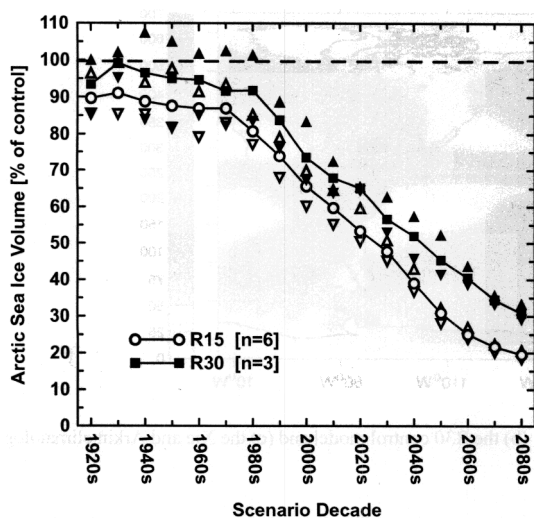


Fig. 7. Time variations of the volume of sea ice simulated to exist poleward of 67°N , expressed as a percentage of that present in a climate change experiment relative to the amount simulated in the corresponding control run. Ensemble mean decadal average values are shown for the six R15 (open circles) and three R30 (solid squares) experiments. Upward and downward pointing triangles indicate the maximum and minimum values of the ensemble members (R15=open triangles, R30=solid triangles).

Differences between the ensemble mean R15 and R30 results seen in Fig. 7 do not appear to be associated with any cold start bias that might have been introduced by including the three longer R15 experiments that had transient forcing begin with 1766 conditions rather than 1866. In fact, for the period 1920–1999, the mean Arctic ice volume for the two groups of R15 experiments differs by only 0.2%, with the average of the trio that began at 1766 actually being slightly greater (85.6%) than that of three experiments whose transient forcings began at scenario year 1866 (85.4%). Over the same 80-year period, the R30 climate change experiments averaged 93.3% of the control model's Arctic sea ice volume.

5. Precipitation

5.1. Control models' precipitation simulations

The globally averaged annual mean precipitation rate, a gross measure of the overall strength of the hydrologic cycle, is modeled reasonably well in both the R15 and R30 models. The average annual global mean precipitation computed over the 18 years of the Xie and Arkin (1997) climatology (a blend of satellite, gauge and model data over the period 1979–1996) is 0.98 m year^{-1} . This compares favorably to the 0.95 m year^{-1} simulated in the R15 control model (averaged over 990 model years). In the R30 control model, the annual mean global precipitation averages 0.91 m year^{-1} (a 315-year mean).

Global mean precipitation increases as the simulated climate warms, bringing the models into even closer agreement with the observational estimates. Averaged over the 1979–1995 period, the ensemble mean global precipitation rate in the R15 climate change experiments is $0.014 \text{ m year}^{-1}$ greater than in the control integration. Similarly, the R30's annual mean precipitation rate averages $0.017 \text{ m year}^{-1}$ greater than its control for the same period.

Maps of annual mean precipitation patterns from the two GFDL control models and the Xie and Arkin climatology appear in Fig. 8. Delworth et al. (2002) present seasonal precipitation maps for the R30 model. Zonal averages of the annual mean precipitation are depicted in Fig. 9. The differences that exist between the R15 and R30 atmosphere–ocean

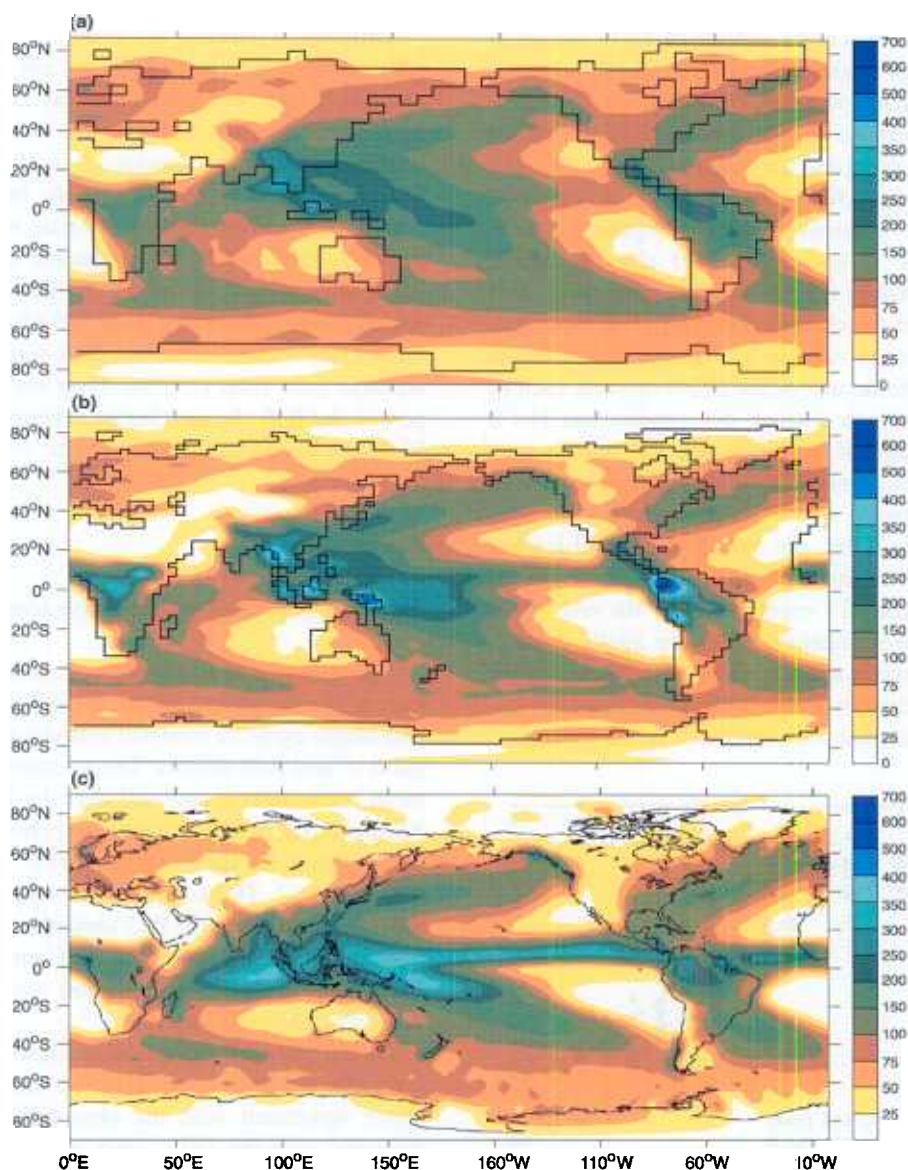


Fig. 8. Annual mean precipitation distributions from (a) the R15 control model, (b) the R30 control model and (c) the Xie and Arkin climatology. Units are centimeters per year. Note irregular contour intervals.

GCMs in Fig. 9 are not dissimilar to those presented by Manabe and Stouffer (1994) for R15 and R30 atmospheric GCMs coupled to mixed layer ocean models.

Pattern correlations reveal that the two control model results examined here are more similar to each other than they are to the observational estimates. The pattern correlation for the R15 and R30 annual mean

precipitation rate fields is 0.86 when the R30 field is interpolated onto the R15 grid point locations before computing the correlation. Somewhat lower pattern correlations are found for the R15-vs.-Xie–Arkin comparison ($r=0.75$) and the R30-vs.-Xie–Arkin comparison ($r=0.74$) (the observational estimates were interpolated to the respective model grid before calculating the spatial correlation).

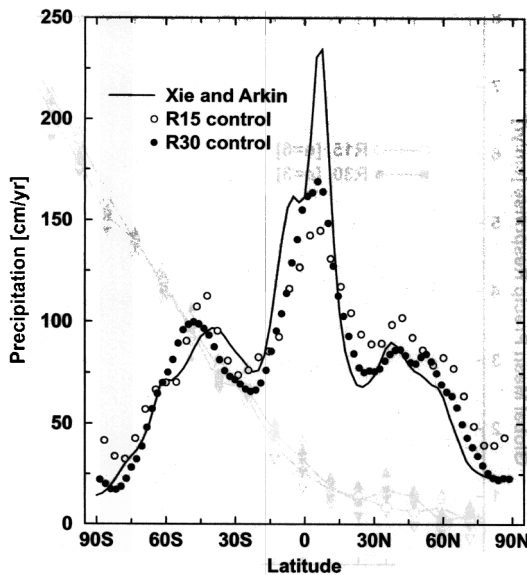


Fig. 9. Zonally averaged annual mean precipitation rates computed from the Xie and Arkin climatology (solid line), the R15 control run (open circles), and the R30 control run (filled circles). The R15 values are averaged over 990 years and the R30 values are averaged over 315 years. Xie and Arkin values are averaged over the period 1979–1996.

When comparing the coupled model-simulated precipitation with the Xie and Arkin data set, one should be mindful that variations in the spatial coverage of the various data sources used to create the observation-based precipitation climatology lead to the largest uncertainties being found over oceans poleward of 60° and in the area of mid-latitude oceanic storm tracks. More generally, limitations associated with observing precipitation, a field with much small-scale variability, leads to uncertainties in global precipitation climatologies. See Xie and Arkin (1997) for a more complete discussion of the strengths and weaknesses of the merged precipitation analysis product.

The higher resolution R30 model yields an improved simulation of some large-scale precipitation features, including the Intertropical Convergence Zone. The R30 model also exhibits more spatial variability than the R15 model. Compared to the Xie and Arkin data, the lower resolution R15 model yields too much precipitation in high latitudes. There is less bias in the R30 model's high-latitude zonal mean precipitation. For example, the Xie and Arkin climatological estimate for the annual precipitation

spatially averaged over the region north of 67°N is $\sim 0.28 \text{ m year}^{-1}$. In contrast, the atmospheric component of the R15 control model yields 0.50 m year^{-1} of Arctic precipitation, while the R30 control model simulates 0.36 m year^{-1} .

Compared to the Xie and Arkin climatology, both of the GFDL models display a tendency to have too little rainfall over low-latitude ocean regions (Fig. 10). Zonal averages of the R30 control run's precipitation rates over low-latitude land exceed climatological estimates, while the R15 model's are comparable to the climatological values. A bias towards precipitation preferentially falling over low-latitude land rather than the ocean is more pronounced in the higher resolution R30 control integration. This is consistent with the R30 model's low-latitude precipitation having higher spatial variability than the R15, as evident in the contrast between high-precipitation areas (e.g., the ITCZ and over some land masses) and drier regions dominated by subsidence being more pronounced in the R30 model than in the R15.

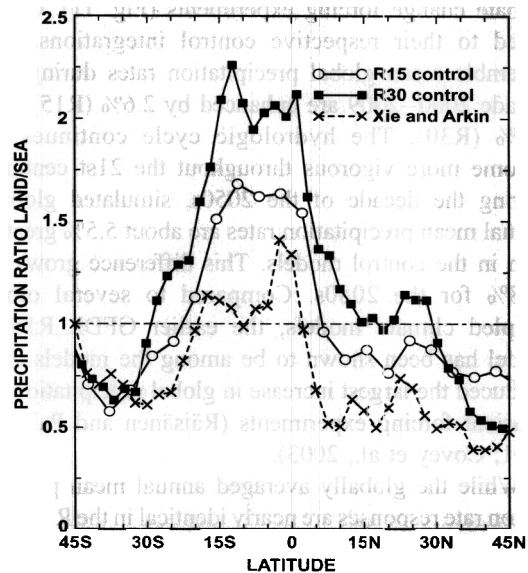


Fig. 10. A comparison of annual mean precipitation rates over land relative to precipitation rates over the ocean. Zonal averages of annual mean precipitation rates over land grid points and over ocean grid points were computed for both the control models and the Xie and Arkin climatology. The ratios were computed as the land precipitation zonal mean divided by the ocean precipitation zonal mean. R15 model results are shown as open circles; the R30 results as solid squares and the Xie and Arkin climatology as \times .

While a better defined ITCZ is not unexpected when going from low to medium resolution, the reasons that both GFDL models exhibit a bias toward too much low-latitude rainfall over land are less clear and would require additional experiments to determine with certainty. Since interactions and feedbacks between the land surface and atmospheric model components can influence many simulated features (see Betts et al., 1996, for a review) one could speculate that the specifics of the soil hydrology, boundary layer, cloud prediction and moist convective adjustment schemes (the latter not being very scale selective), could play a role in yielding the land/sea precipitation bias. That the topography is better resolved in the R30 model also may contribute to increased orographic precipitation in some low-latitude land areas.

5.2. Precipitation response to GHG forcing

The response of the globally averaged annual mean precipitation rate is very similar in the R15 and R30 climate change forcing experiments (Fig. 11). Compared to their respective control integrations, the ensemble mean global precipitation rates during the decade 2000–2009 are enhanced by 2.6% (R15) and 2.8% (R30). The hydrologic cycle continues to become more vigorous throughout the 21st century. During the decade of the 2050s, simulated global, annual mean precipitation rates are about 5.5% greater than in the control models. This difference grows to ~8% for the 2080s. Compared to several other coupled climate models, the earlier GFDL_R15_a model has been shown to be among the models that produced the largest increase in global precipitation in transient forcing experiments (Räisänen and Palmer, 2001; Covey et al., 2003).

While the globally averaged annual mean precipitation rate responses are nearly identical in the R15 and R30 models, substantial differences exist between the zonal mean responses produced by the two models (Figs. 12 and 13). As the simulated climates warm, the R30 model displays a larger precipitation response in the equatorial latitudes than does the R15 model. Confining the area of interest to the zonal band extending from ~4.5°S to 4.5°S, we note that over the period 1990–2014, the R15 model's annual precipitation rate averages 0.04 m year⁻¹ above that simulated in the

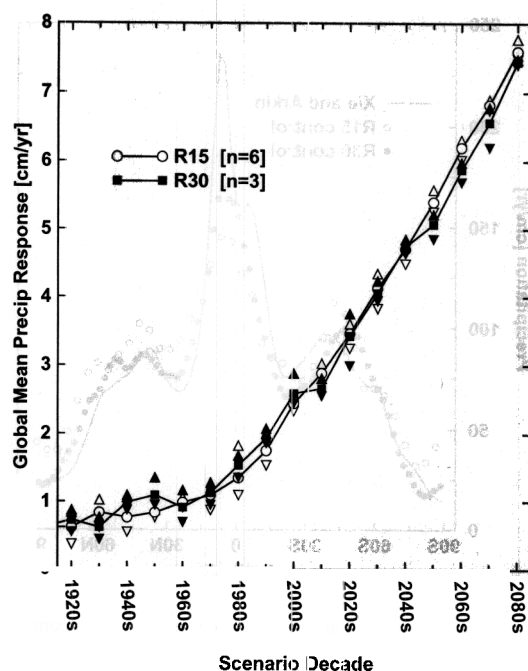


Fig. 11. Time variations of the modelled precipitation rate response to the imposed climate change forcing scenario. Decadal mean precipitation rate responses are plotted, expressed as a deviation of that simulated in a climate change experiment relative to that simulated in the corresponding control run. Ensemble mean decadal average values are shown for the six R15 (open circles) and three R30 (solid squares) experiments. Upward and downward pointing triangles indicate the maximum and minimum values of the ensemble members (R15 = open triangles, R30 = solid triangles).

control (a 3.3% increase). In the R15 climate change experiments, this response grows to an average of 0.12 m year⁻¹ for the period 2065–2089 (an 8.9% increase). In contrast, the R30 model's annual mean precipitation rate in this equatorial zone is already 0.12 m year⁻¹ greater than in its control during the 1990–2014 averaging period (a 7.7% increase). Averaged over the period 2065–2089, the R30 model's equatorial precipitation response is 0.36 m—three times greater than that simulated in the R15 model for the same time and a 23.4% increase over the R30 control. The largest increases in R30 precipitation field occur in a region centered near the Equator and 180° longitude, with a lobe extending southeastward to Tahiti.

In the zonal mean, reductions in precipitation can be seen in the subtropical latitudes of the R30 climate change simulations. By the end of the integrations, an

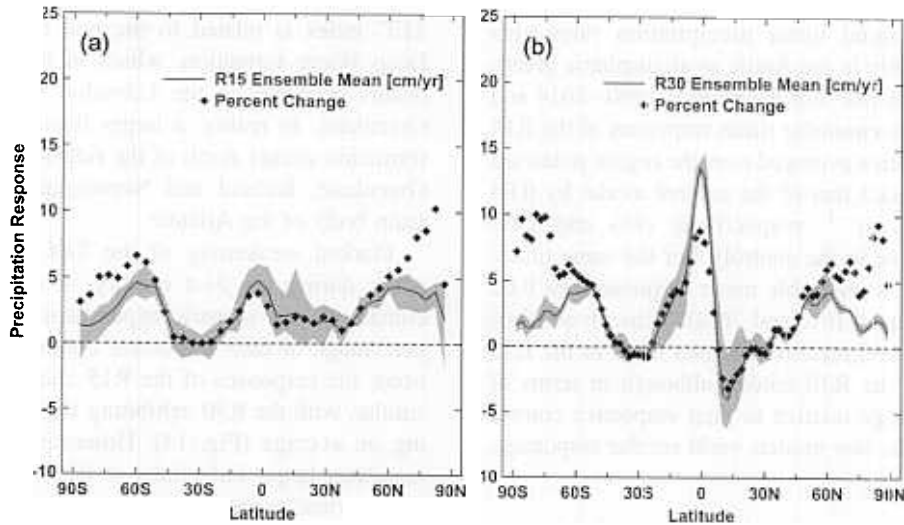


Fig. 12. Zonal mean precipitation responses for the (a) R15 and (b) R30 climate change experiments averaged over the scenario time period 1990–2014. Ensemble mean values of the response in units of centimeters per year are shown by the solid black lines. Gray areas encompass the range of zonal mean precipitation responses produced by the ensemble members. For each climate change experiment, responses were calculated by averaging zonal mean precipitation rates over the period of interest, and then subtracting the average zonal mean value computed over the corresponding 25-year period of the control model. Ensemble means were calculated by averaging the precipitation responses of the six R15 and three R30 experiments. Diamonds denote the ensemble mean responses expressed as a percent change relative to the control model.

area where precipitation decreases by more than 0.40 m year^{-1} is simulated for a part of the western South Pacific, extending southeastward from the Solomon Sea to a point near 25°S and 180° longitude. Such a well-defined feature does not appear in the R15. The changes in the R30 model's Pacific low-latitude

precipitation patterns are consistent with the region of strongest precipitation moving eastward during the climate change scenario experiments, from the western tropical Pacific towards the dateline as the surface waters warm more in the eastern and central tropical Pacific than in the western tropical Pacific.

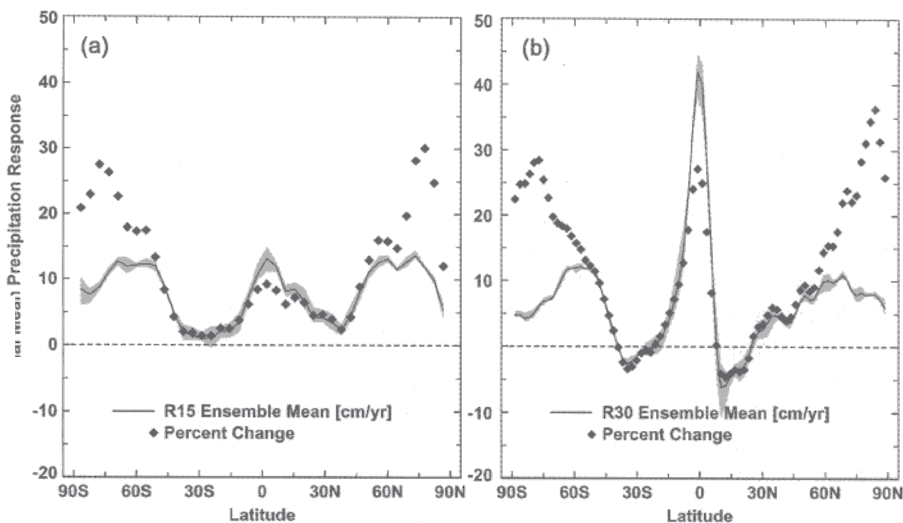


Fig. 13. Same as Fig. 12 but averaged for the time period 2065–2089. Note that the y-axis scale is different in Fig. 12.

Modeled annual mean precipitation rates also increase markedly in the Arctic as atmospheric greenhouse gas levels rise. For the periods 1990–2014 and 2065–2089, the ensemble mean responses of the R15 model experiments averaged over the region poleward of 67°N exceeded that of the control model by 0.04 and 0.12 m year^{-1} , respectively (8% and 24% increases relative to the control). For the same times, the R30 model's ensemble mean responses are 0.02 and 0.09 m year^{-1} (6% and 26%). Thus, in absolute terms, Arctic precipitation increases more in the R15 model than in the R30 model, although in terms of percentage change relative to their respective control experiments, the two models yield similar responses.

6. Atlantic meridional overturning circulation

The potential for the North Atlantic thermohaline circulation (THC) to weaken in response to greenhouse gas-induced climate change and the possible implications of such a weakening on regional and global climate have intrigued researchers for several years (Broecker, 1987). This meridional overturning circulation, characterized by northward-moving warm surface waters and a return flow of cooler, salty water at depth, plays an important role in poleward heat transport in the climate system. A wide range of THC responses has been simulated in coupled climate model experiments conducted at various research centers (Kattenberg et al., 1996), with some models exhibiting dramatic decreases in the strength of the overturning circulation, while others show only slight weakening.

The strength of the North Atlantic THC simulated in control experiments also varies among different coupled models (Gates et al., 1996; McAvaney et al., 2001), with many being outside the range of 13–18 Sverdrups ($1 \text{ Sv} = 10^6 \text{ m}^3 \text{ s}^{-1}$) estimated to be representative of late 20th century conditions (Schmitz and McCartney, 1993). The strength of the THC in the R15 coupled model examined here averages 14.9 Sv, while the R30 control model's THC averages 25.6 Sv over the period studied. The index we use to indicate the THC strength is the maximum value of the stream function representing the meridional circulation computed across the North Atlantic from the annual mean northward component of a model's velocity field. The

THC index is related to the rate of North Atlantic Deep Water formation, which in these two models occurs primarily in the Labrador Sea and south of Greenland. In reality, a larger fraction of deepwater formation occurs north of the ridges that separate the Greenland, Iceland and Norwegian Seas from the main body of the Atlantic.

Marked weakening of the THC is simulated to occur during the 21st century in all of the GFDL climate change scenario experiments. Expressed as a percentage of their respective control model integrations, the responses of the R15 and R30 models are similar, with the R30 exhibiting slightly less weakening on average (Fig. 14). However, the R30 model simulates larger reductions in the overturning circulation when expressed as the change in volume per unit time. The ensemble mean responses of both models reveal less than a 10% decrease in the THC

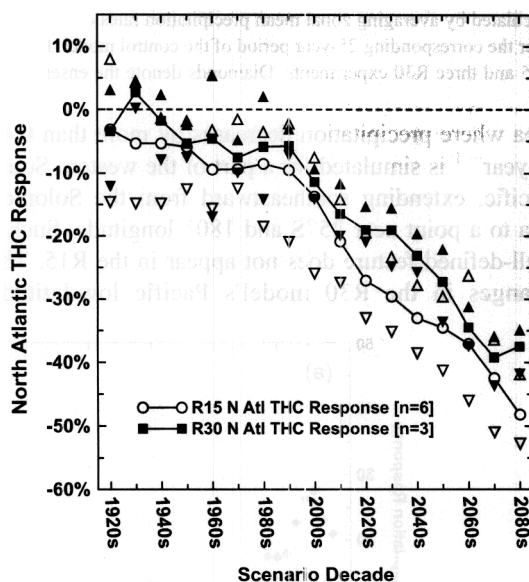


Fig. 14. Time variations of the North Atlantic meridional overturning circulation's response to the imposed climate change forcing scenario. Decadal mean responses are plotted, expressed as a percentage change relative to the long-term mean of the corresponding control run. Ensemble mean decadal average values are shown for the six R15 (open circles) and three R30 (solid squares) experiments. Upward and downward pointing triangles indicate the maximum and minimum values of the ensemble members (R15 = open triangles, R30 = solid triangles). The R15 control model's long-term mean overturning is 14.9 Sv and the long-term mean for the R30 control is 25.6 Sv.

index by the 1990s. More rapid weakening occurs during the 21st century. In the decade of the 2020s (during which the effective CO₂ levels reach twice that of the control model) the R15 model's THC had on average weakened by 27% (4.0 Sv) and the R30 model by 19% (4.9 Sv). By the 2080s, the R15 ensemble mean THC index is 48% (7.2 Sv) less than its control, while the R30 model is 38% (9.6 Sv) weaker than its control.

Relatively large amounts of THC decadal variability are present in the control integrations of the R15 (DL99) and R30 (Delworth et al., 2002) models. This variability is evident in decadal mean responses shown in Fig. 14. During the 17 decades shown, the range (the difference between the largest and smallest responses of the ensemble members) of the six R15 experiments' THC response averaged 2.1 Sv. Among the three sets of R30 decadal mean responses, the range averaged 2.6 Sv. The standard deviation of the time series of the R30 control model's annual mean THC index (2.2 Sv) is greater than that of the R15 control model (0.8 Sv).

As shown in DL99, the R15 model's THC response is insensitive to whether the scenario experiments were initialized with 1765 or 1865 conditions. In fact, over the period 1920–2089, the average THC index of the three scenario experiments that began at 1866 was 0.3 Sv less than that of the three scenario experiments initialized with 1766 radiative forcing conditions. This difference is mostly attributable to one 1866 ensemble member in which the THC began to weaken a couple of decades earlier than in the other R15 climate change scenario experiments.

The question of what surface forcing changes cause the THC to weaken in the R15 transient climate change experiments was addressed by Dixon et al. (1999). They found that changes in surface freshwater fluxes (precipitation, evaporation and runoff from land) are the primary reason that the model's THC weakens, accounting for about two-thirds of the reduction simulated for the latter half of the 21st century. Surface heat flux changes also contribute to a diminishing of the THC's strength, but are of secondary importance. Climate change-induced wind stress variations have minimal impact on the R15 model's THC. Similar analyses that will quantify the impact of the different surface flux changes on the R30 model's THC are

underway (additional model simulations were performed for this ongoing analysis).

As noted in the recent studies by Mikolajewicz and Voss (2000), Gent (2001) and Thorpe et al. (2001), coupled model projections of how the North Atlantic THC will respond to climate change forcing scenarios yield varying results and are dependent upon several factors. That model THC simulations can be sensitive to variations in inter-basin exchange of water vapor, river outflow, sea ice export from the Arctic, model bathymetry and details of regional precipitation and evaporation patterns suggests that additional research is required to reduce the uncertainties associated with projections of the 21st century North Atlantic THC circulation.

7. Summary

In this paper, we compare the responses of two coupled climate models to a specified scenario of transient radiative forcing. Analyses focus on the time extending from the early 20th century through the late 21st century. The two models examined, GFDL R15 and R30 coupled models, combine atmosphere and ocean general circulation models with simpler models of sea ice and land hydrology. Spatial resolution is the primary difference between the two models, with the R15 model having the coarser resolution of the two. The same physical parameterization schemes are used in both models. Rather than relying on a single experiment to define a model's response to the transient forcing scenario, small ensembles of experiments (six for the R15, three for the R30) are examined to better determine the mean response and the range of responses that can be produced by the models.

In many regards, the climate sensitivities of the two models are comparable. The responses of global mean surface air temperature are similar through the early 21st century. Later in the scenarios, the R15 experiments display somewhat more warming than do the R30 experiments. That the R15 results exhibit somewhat greater global warming and more polar amplification of the warming signal is likely in part to be due to the R15 control experiment having a cooler control state than the R30 control experiment. Having been initialized from a control climate with more snow and

ice, the R15 has a greater capacity for positive albedo feedbacks.

Both the R15 and R30 models simulate sizeable reductions in the volume of Arctic sea ice to occur in the 21st century, with the R15 exhibiting a somewhat larger response, both in terms of percentage reduction and the absolute volume of Arctic sea ice decrease.

Control state biases that lead to excessive high-latitude precipitation and too little equatorial rainfall were reduced in going from the coarser resolution R15 model to the R30 model. Increased spatial variability and a more well-defined ITCZ are evident in the R30 model's precipitation field and are likely related to increased atmospheric spatial resolution. Compared to the observational climatology of Xie and Arkin (1997), both control models appear to have a bias in the tropics of too much rainfall over land and too little over the oceans. Global mean precipitation responses to the transient radiative forcing are similar ($\sim 8\%$ increase by the 2080s). However, the R30 experiments have a larger precipitation response near the equator than is evident in the R15 simulations.

The North Atlantic overturning circulation is stronger in the R30 model than in the R15. Both models simulate a marked decrease in the strength of this Atlantic overturning circulation as the climate warms. Expressed as a percentage of the average THC strength of their respective control runs, the R15 model's THC weakens somewhat more than the R30 model's during the 21st century. The North Atlantic THC displays a substantial amount of multi-decadal variability in both models.

Efforts such as CMIP (the Coupled Model Inter-comparison Project) (Covey et al., 2003) that foster the collection and analysis of climate change simulations produced by coupled climate models developed at different institutions have been successful at exposing model-to-model simulation differences. Such analyses can lead to much speculation regarding which differences in the models' formulation and construction are responsible for the differences evident in the model-simulated climates. Often, the specific reasons for the model simulation differences cannot be identified with certainty, because of the many differences in model configurations and the codes used in building the various coupled models. By limiting our focus here to two GFDL coupled models that share the same model code and physical

parameterizations, the prospect for determining the reasons for differences in the two models' climate change responses is improved. However, we find that in some cases additional experiments will be required to make such determinations in an unambiguous and quantitative manner.

For example, it is very likely that, compared to the R30 model, the R15 control experiment's cooler control climate leads to more efficient albedo feedbacks associated with somewhat stronger global warming and polar amplification of the warming signal. However, additional experiments would be needed to isolate and quantify the roles of the modeled sea ice and snow albedo feedback mechanisms. Similarly, with the experiments on hand, one cannot determine quantitatively to what extent the soil hydrology, moist convective adjustment and other parameterization schemes interact with changing spatial resolution to contribute to an apparent bias for too much precipitation to fall over low-latitude land masses.

Such results highlight the value of considering a wide range of factors when developing coupled climate models for use in generating climate change scenario projections. For example, in addition to judging a control experiment by more traditional metrics such as the distribution of surface air temperature and sea ice, one should consider the distribution of snow on the ground and high-latitude albedos, since they can influence the model's climate sensitivity through positive feedback loops. While not a novel observation, an increased appreciation of factors such as these will be useful as the next generation GFDL coupled climate model, one with more complex physical parameterizations and higher spatial resolution, is developed and its simulated climate assessed.

Acknowledgements

We wish to thank our many colleagues who have contributed to the development and analysis of aspects of the global GFDL coupled climate models. Anthony Broccoli and Anthony Rosati provided suggestions that helped improve the paper. We also thank two anonymous reviewers for their thoughtful comments, and Phil Duffy for his editorial patience.

References

- Betts, A.K., Ball, J.H., Beljaars, A.C.M., Miller, M.J., Viterbo, P.A., 1996. The land surface–atmosphere interaction: a review based on observational and global modeling perspectives. *J. Geophys. Res.* 101 (D3), 7209–7225.
- Boer, G.J., Lazare, M., 1988. Some results concerning the effect of horizontal resolution and gravity-wave drag on simulated climate. *J. Climate* 1 (8), 789–806.
- Broecker, W.S., 1987. Unpleasant surprises in the greenhouse? *Nature* 328, 123–126.
- Bryan, K., 1969. Climate and the ocean circulation III. The ocean model. *Mon. Weather Rev.* 97 (11), 806–827.
- Bryan, K., Manabe, S., Spelman, M.J., 1988. Interhemispheric asymmetry in the transient response of a coupled ocean–atmosphere model to a CO₂ forcing. *J. Phys. Oceanogr.* 18 (6), 851–867.
- Covey, C., AchutaRao, K.M., Cubasch U., Jones, P., Lambert, S.J., Mann, M.E., Phillips, T.J., Taylor, K.E., 2003. An overview of results from the Coupled Model Intercomparison Project (CMIP). *Global Planet. Change* 37, 103–133.
- Cox, M.D., 1987. Isopycnal diffusion in a z-coordinate ocean model. *Ocean Model.* 74, 1–5.
- Delworth, T.L., Dixon, K.W., 2000. Implications of the recent trend in the Arctic/North Atlantic Oscillation for the North Atlantic thermohaline circulation. *J. Climate* 13 (21), 3721–3727.
- Delworth, T.L., Knutson, T.R., 2000. Simulation of early 20th century global warming. *Science* 287 (5461), 2246–2250.
- Delworth, T.L., Stouffer, R.J., Dixon, K.W., Spelman, M.J., Knutson, T.R., Broccoli, A.J., Kushner, P.J., Wetherald, R.T., 2002. Simulation of climate variability and change by the GFDL R30 coupled climate model. *Clim. Dyn.* 19 (7), 555–574.
- Dixon, K.W., Lanzante, J.R., 1999. Global mean surface air temperature and North Atlantic overturning in a suite of coupled GCM climate change experiments. *Geophys. Res. Lett.* 26 (13), 1885–1888.
- Dixon, K.W., Delworth, T.L., Spelman, M.J., Stouffer, R.J., 1999. The influence of transient surface fluxes on North Atlantic overturning in a coupled GCM climate change experiment. *Geophys. Res. Lett.* 26 (17), 2749–2752.
- Gates, W.L., Henderson-Sellers, A., Boer, G.J., Folland, C.K., Kitoh, A., McAvaney, B.J., Semazzi, F., Smith, N., Weaver, A.J., Zeng, Q.-C., 1996. Climate models—evaluation. In: Houghton, J.J., Meiro Filho, L.G., Callander, B.A., Harris, N., Kattenberg, A., Maskell, K. (Eds.), *Climate Change 1995: The Science of Climate Change*. Cambridge Univ. Press, Cambridge, UK, pp. 229–284.
- Gent, P., 2001. Will the North Atlantic Ocean thermohaline circulation weaken during the 21st century? *Geophys. Res. Lett.* 28 (6), 1023–1026.
- Gregory, J.M., Church, J.A., Boer, G.J., Dixon, K.W., Flato, G.M., Jackett, D.R., Lowe, J.A., O'Farrell, S.P., Roeckner, E., Russell, G.L., Stouffer, R.J., Winton, M., 2001. Comparison of results from several AOGCMs for global and regional sea level change 1900–2100. *Clim. Dyn.* 18 (3/4), 225–240.
- Hansen, J., Sato, M., Ruedy, R., Lacis, A., Oinas, V., 2000. Global warming in the twenty-first century: an alternative scenario. *Proc. Natl. Acad. Sci.* 97, 9875–9880.
- Hasselmann, K., Sausen, R., Maier-Reimer, E., Voss, R., 1993. On the cold start problem in transient simulations with coupled atmosphere–ocean models. *Clim. Dyn.* 9, 53–61.
- Haywood, J.M., Stouffer, R.J., Wetherald, R.T., Manabe, S., Ramaswamy, V., 1997. Transient response of a coupled model to estimated changes in greenhouse gas and sulfate concentrations. *Geophys. Res. Lett.* 24 (11), 1335–1338.
- Holloway, G., Sou, T., 2001. Has Arctic sea ice rapidly thinned? *J. Climate* 15 (13), 1691–1701.
- Ingram, W.J., Wilson, C.A., Mitchell, J.F.B., 1989. Modeling climate change: an assessment of sea ice and surface albedo feedbacks. *J. Geophys. Res.* 94 (D6), 8609–8622.
- Intergovernmental Panel on Climate Change (IPCC), 1990. In: Houghton, J.T., Jenkins, G.J., Ephraums, J.J. (Eds.), *Climate Change: The IPCC Scientific Assessment*. Cambridge Univ. Press, Cambridge, UK, p. 365.
- Intergovernmental Panel on Climate Change (IPCC), 1996. In: Houghton, J.T., Meiro Filho, L.G., Callander, B.A., Harris, N., Kattenberg, A., Maskell, K. (Eds.), *Climate Change 1995: The Science of Climate Change. Contribution of Working Group I to the Second Assessment Report of the Intergovernmental Panel on Climate Change*. Cambridge Univ. Press, Cambridge, UK, p. 572.
- Intergovernmental Panel on Climate Change (IPCC), 2001. In: Houghton, J.T., Ding, Y., Griggs, D.J., Noguer, M., van der Linden, P.J., Xiaosu, D. (Eds.), *Climate Change 2001: The Scientific Basis Contribution of Working Group I to the Third Assessment Report of the Intergovernmental Panel on Climate Change (IPCC)*. Cambridge Univ. Press, Cambridge, UK, p. 944.
- Kattenberg, A., Giorgi, F., Grassl, H., Meehl, G.A., Mitchell, J.F.B., Stouffer, R.J., Tokioka, T., Weaver, A.J., Wigley, T.M.L., 1996. Climate models—projections of future climate. In: Houghton, J.J., Meiro Filho, L.G., Callander, B.A., Harris, N., Kattenberg, A., Maskell, K. (Eds.), *Climate Change 1995: The Science of Climate Change*. Cambridge Univ. Press, Cambridge, UK, pp. 285–357.
- Knutson, T., Manabe, S., 1998. Model assessment of decadal variability and trends in the tropical Pacific Ocean. Preprints, The Ninth Symposium on Global Change Studies and Namias Symposium on the Status and Prospects for Climate Prediction. American Meteorological Society, Boston, MA, pp. 216–219.
- Knutson, T.R., Manabe, S., Gu, D., 1997. Simulated ENSO in a global coupled ocean–atmosphere model: multidecadal amplitude modulation and CO₂ sensitivity. *J. Climate* 10 (1), 138–161.
- Knutson, T.R., Delworth, T.L., Dixon, K.W., Stouffer, R.J., 1999. Model assessment of regional surface temperature trends (1949–1997). *J. Geophys. Res.* 104 (D24), 30981–30996.
- Leggett, J., Pepper, W.J., Swart, R.J., 1992. Emissions scenarios for the IPCC: an update. In: Houghton, J.T., Callander, B.A., Varney, S.K. (Eds.), *Climate Change 1992: The Supplementary Report to the IPCC Scientific Assessment*. Cambridge Univ. Press, Cambridge, UK, pp. 69–95.
- Levitus, S., Antonov, J.I., Wang, J., Delworth, T.L., Dixon, K.W.,

- Broccoli, A.J., 2001. Anthropogenic warming of Earth's climate system. *Science* 292 (5515), 267–270.
- Lindberg, C., Broccoli, A.J., 1996. Representation of topography in spectral climate models and its effect on simulated precipitation. *J. Climate* 9 (11), 2641–2659.
- Manabe, S., 1969. Climate and the ocean circulation: 1. The atmospheric circulation and the hydrology of the earth's surface. *Mon. Weather Rev.* 97 (11), 739–774.
- Manabe, S., Stouffer, R.J., 1994. Multiple-century response of a coupled ocean–atmosphere model to an increase of atmospheric carbon dioxide. *J. Climate* 7 (1), 5–23.
- Manabe, S., Smagorinsky, J., Strickler, R.F., 1965. Simulated climatology of a general circulation model with a hydrologic cycle. *Mon. Weather Rev.* 93 (12), 769–798.
- Manabe, S., Bryan, K., Spelman, M.J., 1990. Transient response of a global ocean–atmosphere model to a doubling of atmospheric carbon dioxide. *J. Phys. Oceanogr.* 20 (5), 722–749.
- Manabe, S., Stouffer, R.J., Spelman, M.J., Bryan, K., 1991. Transient responses of a coupled ocean–atmosphere model to gradual changes of atmospheric CO₂. Part I. Annual mean response. *J. Climate* 4 (8), 785–818.
- May, W., Roeckner, E., 2001. A time-slice experiment with the ECHAM4 AGCM at high resolution: the impact of horizontal resolution on annual mean climate change. *Clim. Dyn.* 17 (5–6), 407–420.
- McAvaney, B.J., Covey, C., Joussaume, S., Kattsov, V., Kitoh, A., Pitman, A.J., Weaver, A.J., Wood, R.A., Zhao, Z.-C., 2001. Model evaluation. In: Houghton, J.T., Ding, Y., Griggs, D.J., Noguer, M., van der Linden, P.J., Xiaosu, D. (Eds.), *Climate Change 2001: The Scientific Basis Contribution of Working Group I to the Third Assessment Report of the Intergovernmental Panel on Climate Change (IPCC)*. Cambridge Univ. Press, Cambridge, UK, pp. 471–523.
- Mikolajewicz, U., Voss, R., 2000. The role of the individual air–sea flux components in CO₂-induced changes of the ocean's circulation and climate. *Clim. Dyn.* 16, 627–642.
- Milly, P.C.D., Wetherald, R.T., Dunne, K.A., Delworth, T.L., 2002. Increasing risk of great floods in a changing climate. *Nature* 415 (6871), 514–517.
- Moritz, R.E., Bitz, C.M., 2000. Northern Hemisphere sea ice extent. *Science* 288, 927a.
- Pacanowski, R., Dixon, K., Rosati, A., 1991. The GFDL Modular Ocean Model Users Guide version 1. GFDL Ocean Group Technical Report No. 2, NOAA/Geophysical Fluid Dynamics Laboratory, Princeton, NJ.
- Räisänen, J., 2001. CO₂-induced climate change in CMIP2 experiments: quantification of agreement and role of internal variability. *J. Climate* 14 (9), 2088–2104.
- Räisänen, J., Palmer, T.N., 2001. A probability and decision-model analysis of a multimodel ensemble of climate change simulations. *J. Climate* 14 (15), 3212–3226.
- Rind, C., Healy, R., Parkinson, C., Martinson, D., 1995. The role of sea ice in 2 × CO₂ climate model sensitivity. Part I. The total influence of sea ice thickness and extent. *J. Climate* 8, 449–463.
- Rind, C., Healy, R., Parkinson, C., Martinson, D., 1997. The role of sea ice in 2 × CO₂ climate model sensitivity. Part II. Hemispheric dependencies. *Geophys. Res. Lett.* 24 (212), 1491–1494.
- Rothrock, D.A., Yu, Y., Maykut, G.A., 1999. Thinning of the Arctic sea ice cover. *Geophys. Res. Lett.* 26 (23), 3469–3472.
- Schmitz, W.J., McCartney, M.S., 1993. On the North Atlantic circulation. *Rev. Geophys.* 31 (1), 29–49.
- Senior, C.A., 1995. The dependence of climate sensitivity on the horizontal resolution of a GCM. *J. Climate* 8 (11), 2860–2880.
- Spelman, M.J., Manabe, S., 1984. Influence of oceanic heat transport upon the sensitivity of a model climate. *J. Geophys. Res.* 89 (C1), 571–586.
- Stouffer, R.J., Dixon, K.W., 1998. Initialization of coupled models for use in climate studies: a review. In *Research Activities in Atmospheric and Oceanic Modelling*, Report No. 27, WMO/TD-No. 865. World Meteorological Organization, Geneva, Switzerland, pp. I.1–I.8.
- Stouffer, R.J., Manabe, S., Bryan, K., 1989. Interhemispheric asymmetry in climate response to a gradual increase of atmospheric CO₂. *Nature* 342, 660–662.
- Thorpe, R.B., Gregory, J.M., Johns, T.C., Wood, R.A., Mitchell, J.F.B., 2001. Mechanisms determining the Atlantic thermohaline circulation response to greenhouse gas forcing in a non-flux-adjusted coupled climate model. *J. Climate* 14 (14), 3102–3116.
- Vinnikov, K.Y., Robock, A., Stouffer, R.J., Walsh, J.E., Parkinson, C.L., Cavalieri, D.J., Mitchell, J.F.B., Garrett, D., Zakharov, V.F., 1999. Global warming and Northern Hemisphere sea ice extent. *Science* 286 (5446), 1934–1937.
- Wetherald, R.T., Stouffer, R.J., Dixon, K.W., 2001. Committed warming and its implications for climate change. *Geophys. Res. Lett.* 28 (8), 1535–1538.
- Winsor, P., 2001. Arctic sea ice thickness remained constant during the 1990s. *Geophys. Res. Lett.* 28 (6), 1039–1041.
- Xie, P., Arkin, P.A., 1997. Global precipitation: a 17-year monthly analysis based on gauge observations, satellite estimates, and numerical model outputs. *Bull. Am. Meteorol. Soc.* 78, 2539–2558.